Rafting-Enabled Recovery Avoids Recrystallization in 3D-Printing-Repaired Single-Crystal Superalloys

Kai Chen[1], Runqiu Huang[1], Yao Li[2], Sicong Lin[1], Wenxin Zhu[1], Nobumichi Tamura[3], Ju Li[4,*], Zhi-Wei Shan[1,*], Evan Ma[5,*]

1. Center for Advancing Materials Performance from the Nanoscale, State Key Laboratory for Mechanical Behavior of Materials, Xi'an Jiaotong University, Xi'an, Shaanxi 710049, P.R. China.

2. School of Materials Science and Engineering, Chang'an University, Xi'an, Shaanxi 710064, P.R. China.

3. Advanced Light Source, Lawrence Berkeley National Laboratory, Berkeley, CA 94720, USA.

4. Departments of Nuclear Science and Engineering and Materials Science and Engineering, Massachusetts Institute of Technology, Cambridge, MA 02139, USA.

5. Department of Materials Science and Engineering, Johns Hopkins University, Baltimore, MD 21218, USA.

E-mail addresses: kchenlbl@gmail.com (K. Chen), ema@jhu.edu (E. Ma), zwshan@xjtu.edu.cn (Z.-W. Shan), liju@mit.edu (J. Li)

Abstract

The repair of damaged Ni-based superalloy single-crystal turbine blades has been a long-standing challenge. Additive manufacturing is a promising route to this end, but a formidable obstacle is that recrystallization seems inevitable in the dislocation-riddled heat-affected zone, bringing forth new grains that degrade the high-temperature creep properties. Here we design a post-3D-printing recovery protocol that eliminates the driving force for recrystallization, namely the stored energy associated with the high dislocation content, prior to standard solution treatment and aging. The post-electron-beam-melting, pre-solution recovery via sub-solvus annealing is rendered possible by the rafting of γ' particles that facilitates dislocation rearrangement and annihilation. The rafted microstructure is removed after solution annealing, leaving behind a damage-free single crystal with uniform γ' precipitates that is indistinguishable from the the rest of the turbine blade. This discovery offers a practical means to keep 3D-printed parts from recrystallizing into a polycrystalline microstructure, paving the way for additive manufacturing to repair, restore and reshape any superalloy single crystal product.

Introduction

Modern turbine blades are made of superalloy single crystals (SXs), strengthened by cuboidal precipitates of ordered γ′-phase in the γ-phase matrix [1]. SX Ni-based superalloys outperform their polycrystalline counterparts by a large margin, in many aspects including the resistance to creep, fatigue, and oxidation [2], by eliminating most of the defects that form during blade casting. These high-value SX blades are nonetheless subject to surface damage and cracking upon extensive service in harsh environments. It is thus critical to find a way to repair the damaged surface while keeping their single crystalline nature as well as the desired uniform γ/γ′ microstructure. Such a successful repair will extend the life of turbine blades and reduce the overall cost significantly.

The versatile 3D printing route emerged in recent years appears to be a powerful option towards this goal [3]. Via "epitaxial" deposition of the alloy, one layer at a time, additive manufacturing can preserve the crystallographic orientation of the substrate SX [4–11]. However, as 3D-printing involves fast cooling, the γ′ precipitated are excessively small with uneven sizes and rounded corners, and hence less stable during high-temperature service. More importantly, a high density of dislocations build up in the heat-affected zone (HAZ), due to unavoidable (often local) deformation under high thermal stresses during printing [12,13]. Upon solution treatment at elevated temperatures, these regions riddled with defects readily undergoes recrystallization (RX) [14] that renders the microstructure polycrystalline, which would significantly degrade the high temperature creep performance of blades (Figure S1 in Supporting Information) [2].

These shortcomings are in fact characteristic of all 3D-printed superalloys [15], such that the repaired part is no longer as strong as the original SX. There is thus a pressing need to conceive an innovative treatment that can resolve this problem.

To this end, our strategy is to design post-3D-printing annealing to reduce the driving force for recrystallization that ruins the SX structure. That is, we aim to remove the accumulated dislocations through a recovery heat treatment (HT) before the standard solution treatment and aging HT. However, conventional wisdom is that recovery is difficult to realize in Ni-based superalloys for mainly two reasons. First, the stacking fault energy of Ni-based superalloys (<~20 mJ/m^2) [16,17] is much lower than that of pure Ni (125 mJ/m^2) [18] and Al (166 mJ/m^2) [19]. A low stacking fault energy promotes the unit dislocations to dissociate into partial dislocations, hampering their climb and cross slip, the basic mechanisms for recovery [19,20]. Second, the closely spaced γ′ particles impede the motion of stored dislocations and hence prevent their annihilation at temperatures below the γ′ solvus [19,21,22]. If, instead, the alloy is heated to temperatures above the γ′ solvus, RX sets in quickly well before the stored defects get effectively removed via recovery [20–23]. Such an RX scenario is demonstrated in Figure 1 (standard solution HT).

In this paper, we demonstrate a novel HT process to produce a repaired single crystal with indistinguishable γ/γ′ microstructure from the interior. Prior to standard solution annealing where all the γ′ disappear, other defects (with associated excess energy) accumulated in the HAZ can already be programmed to be relieved by taking advantage of rafting-facilitated recovery, through an HT step of annealing at an appropriate sub-solvus temperature. During such recovery annealing prior to solution HT, rafted microstructure forms in the HAZ, opening pathways to dislocation rearrangement and annihilation. This greatly reduces the dislocation density, such that in subsequent solution and aging HT, using standard protocol normally used, RX does not get triggered to nucleate new grains.

Results

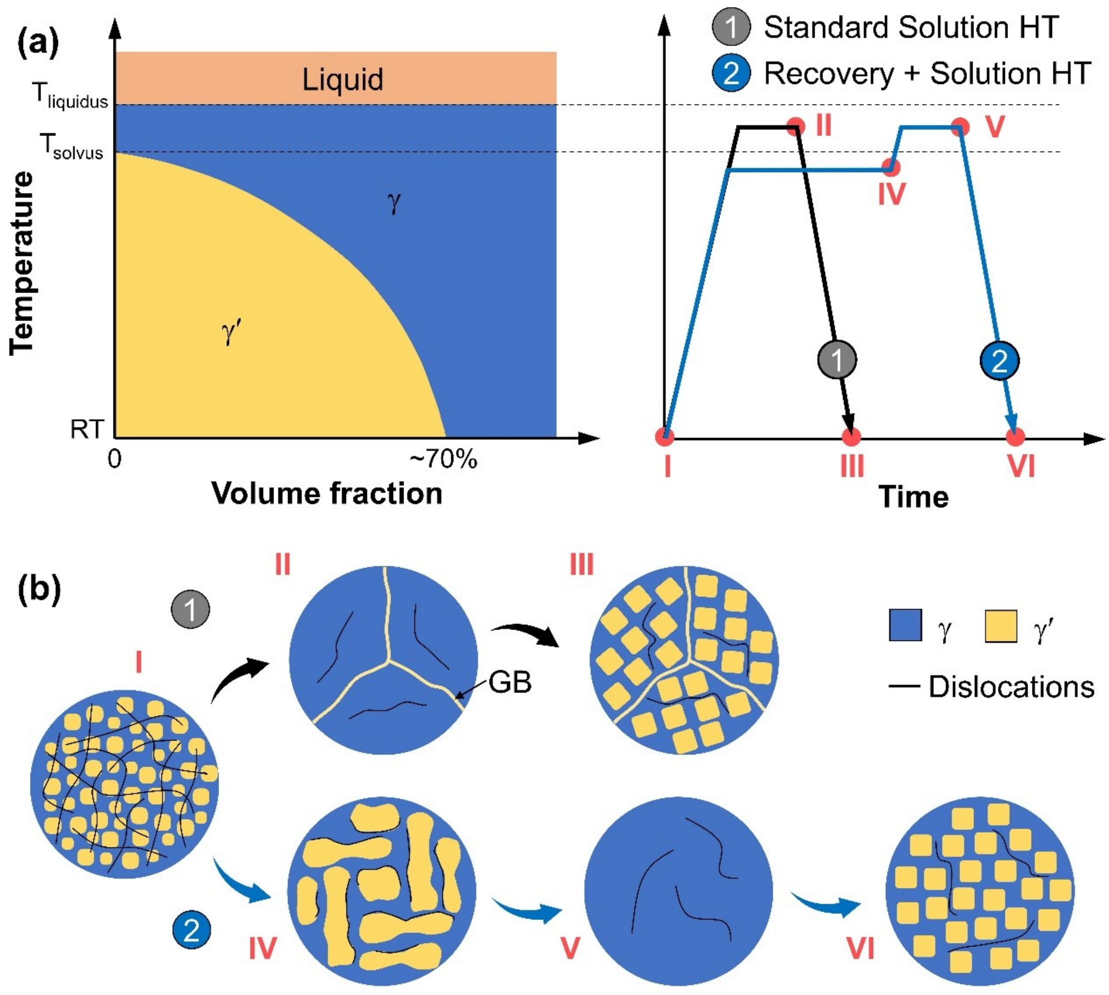

Figure 1 Microstructural evolution of 3D printed Ni-based single crystals induced by standard solution HT, in comparison with our novel HT incorporating recovery annealing. (a) Standard solution HT involves one-step annealing between the solvus and liquidus temperatures, while our new HT protocol includes a recovery annealing procedure prior to solution HT. (b) RX is triggered by the standard

solution HT, but preempted by the new HT.

Electron-beam melting (EBM) with no powder feeding was carried out as an analogue to 3D-printing repairing on AM3, a first-generation SX Ni-based superalloy used as a model in this study. The electron beam was focused and programmed for line scans on the substrate (base metal, BM) surface of [001] cast SX boule to generate fusion zones (FZs). Figure 2 shows the morphology of the EBM sample and the crystal orientation distribution before and after HT using different protocols. In the low-magnification image, Figure 2a, three regions can be readily distinguished: unaffected BM, HAZ, and FZ. The crystal orientation is the same throughout the as-prepared EBM sample, from the BM to the HAZ to the FZ (Figure 2b). After solution HT at 1300 ºC for 30 min without prior recovery annealing, RX grains and high-angle grain boundaries are clearly observed in both HAZ and FZ (Figure 2c). In contrast, after our new 1100 ºC recovery annealing for 6 h prior to standard HT, the electron backscatter diffraction (EBSD) map shows no detectable RX grains (Figure 2d). In other words, the newly developed HT protocol fulfills the “keeping the single crystal” requirement. The other requirement that needs to be accomplished simultaneously is the “uniform γ′ microstructure”.

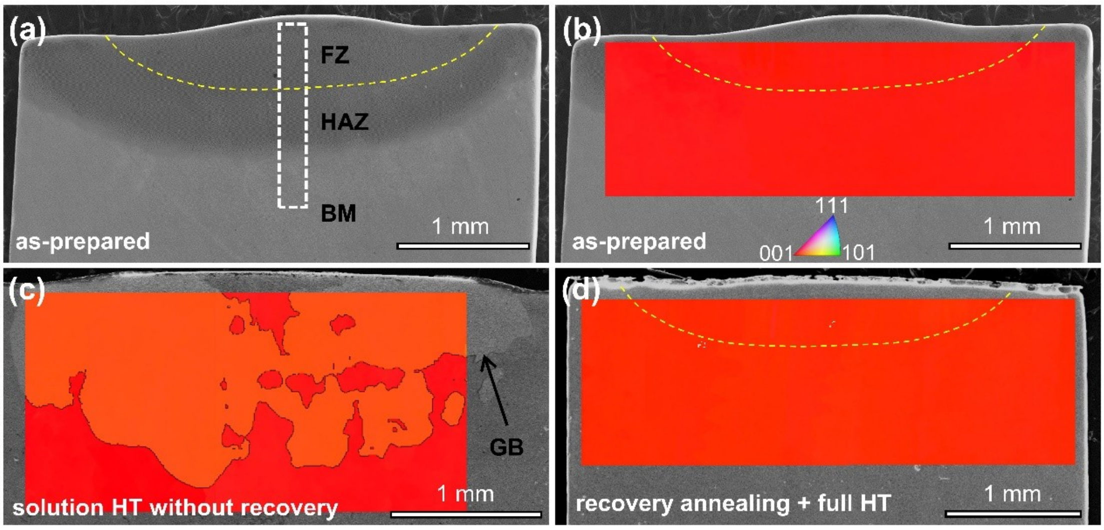

Figure 2 EBM samples before and after different HT protocols. (a) Three regions are visible in the cross-sectional scanning electron microscope (SEM) image of the as-prepared sample: fusion zone (FZ), heat-affected zone (HAZ), and unaffected base metal (BM). EBSD orientation maps indicate that (b) the as-prepared EBM sample is a single crystal, but (c) RX occurs and high-angle grain boundaries are generated upon solution HT at 1300 °C for 0.5 h, while (d) the RX is successfully prevented to keep the single crystalline nature by applying a recovery HT at 1100 °C for 6 h before standard HT.

The EBM sample (Figure 2b) without HT does not fit the bill in this regard. There the fast cooling rate experienced produces not only much finer dendrites in the FZ compared to the cast counterpart, but also much smaller γ′ precipitates - the average size is < 50 nm (Figure 3a), only a quarter of that in the BM. A microstructure gradient is observed in the HAZ (in between the FZ and the BM). The upper HAZ near the fusion line has experienced a temperature sufficiently high to dissolve all the primary γ′. Thus the small particles in the upper HAZ are re-precipitated γ′, quite similar to those in the FZ. Moving down away from the fusion line, the peak temperature is lower and the period of time that the local temperature is above the γ′ solvus is shorter, such that the primary γ′ only dissolves partially. The subsequent re-precipitation at lowered temperatures forms fine secondary γ′. Together they constitute a bimodal γ′ size distribution. The population of the secondary γ′ decreases gradually with increasing distance, becoming completely undetectable in the region about 300 μm away from the fusion line, leaving only cuboidal primary γ′ with side length in the 200 – 300 nm range.

After EBM, the crystal is riddled with dislocations and the elastic strain associated with them is distributed in an inhomogeneous manner. To see the latter, we have taken synchrotron X-ray microdiffraction (μXRD) across the FZ and the HAZ, covering an area of 80 μm (horizontal) × 1150 μm (vertical), as indicated using the boxed rectangle in Figure 2a, at 2 μm spatial resolution. From the orientation inverse pole figure (IPF) maps (Figure S2 in Supporting Information), it appears that the entire scanned area remains a single crystal and the dendrite growth is along the [001] direction. The vertical and horizontal components of the elastic strain tensor, denoted as ε_v and ε_h, respectively, are displayed in Figure 3b. In all regions from the BM through the HAZ to the FZ, these strains are found to vary considerably in magnitude from location to location, and even change sign. The BM substrate is under tension in the vertical direction but is compressed in the horizontal direction; this is believed to be related to the pre-printing thermal history of the superalloy. The opposite is observed for strains in the HAZ: ε_h is tensile while ε_v is compressive. The transition from the BM to the HAZ is smooth and gradual. Both ε_h and ε_v change sign near the BM/HAZ interface. ε_h and ε_v reach their peak magnitudes at the HAZ/FZ interface, and then decrease together upon entering the FZ. The magnitude of the strain is highly variable in the FZ, and changes sign from the interdendritic regions to dendrite cores, probably due to non-uniform chemical distribution. A high density of dislocations in the HAZ is reflected by the obviously-broadened Laue peak width, see the colored peak width map in Figure 3d (although the dislocation density is difficult to quantify accurately from the peak width). In the FZ, the peak width map also exhibits fine stripe features, presumably attributable to the chemical and microstructural heterogeneities between dendrite cores and interdendritic regions. This evidence of a large population of dislocations in many local regions is consistent with the observation in the transmission electron microscope (TEM) image of Figure 3e, in which the dislocation density is measured to be about 8×10^{14} m^{-2}. This value is for a small local region, but from the colored peak width map the dislocation density is inhomogeneous and should be higher in many other regions of the HAZ. Similar to previous reports for cast materials [24], the BM is almost defect free (Figure 3f).

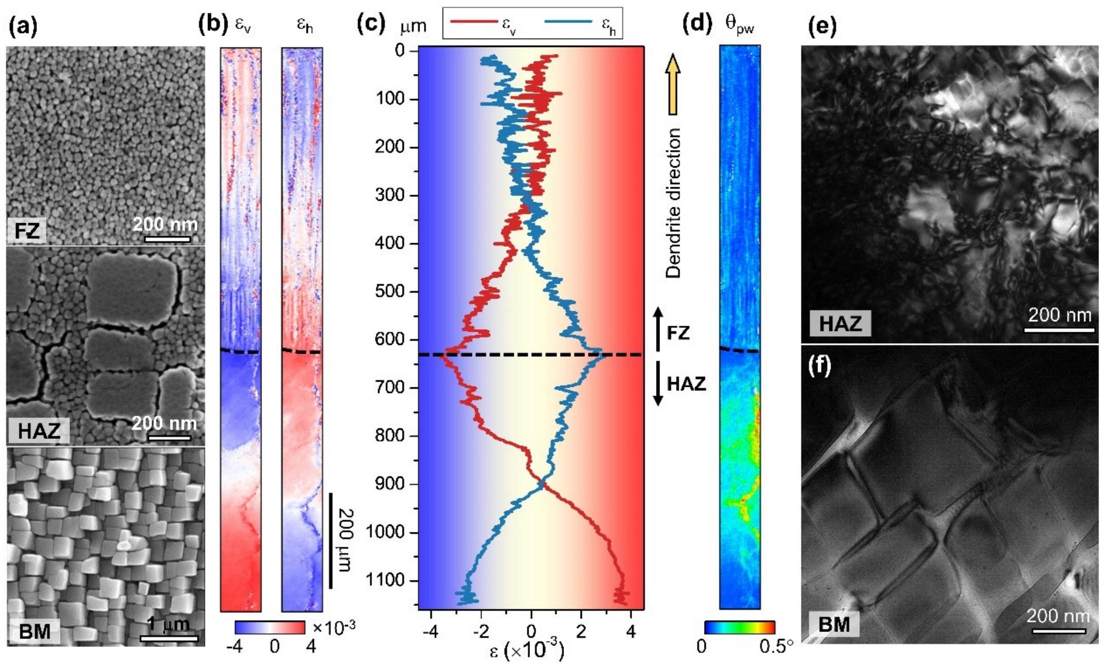

Figure 3 Inhomogeneous distributions of γ′ morphology, elastic strain and dislocations in the EBM sample. (a) Distinctly different γ′ morphologies in the FZ, HAZ, and BM, as displayed in their corresponding SEM images. (b) 2D and (c) 1D lattice elastic strain as well as (d) diffraction peak width

maps indicate non-uniform deformation. The yellow-red region in (d) is believed to represent a dislocation density of > 8 × 10^{14} m^{-2}. The fusion line is marked using a dashed line in (b-d). TEM images indicate that dislocations of high density are present in the HAZ (e), while the BM is almost defect free (f).

We stress again that the dislocations and elastic energy stored are the root cause that drives RX upon the ensuing solutionizing treatment. After the EBM specimen was solution treated at 1300 °C for 30 min, EBSD found RX grains in not only the HAZ but also the FZ (Figure 2b). Shortening of the solution treatment time reduced the area fraction of the RX grains, but was not able to avoid RX, unless the solution treatment is conducted at a temperature well below that needed to reach complete solid solution. Such a temperature, however, would not be able to solutionize the interdendritic region, where the elements promoting γ′ formation are known to be enriched and thus the γ′ solvus temperature is higher than that in the dendrite cores. In other words, without the proposed pre-solution recovery annealing, either RX occurs (at super-solvus temperatures) or the solution treatment is ineffective (at sub-solvus temperatures) to remove the chemical and microstructural heterogeneities from dendrites.

After incorporating our recovery annealing before solution HT, the microstructure becomes completely different from not only the reference sample (full HT after EBM without recovery annealing; as seen in Figure 2c, there RX is obvious, although the precipitates inside the grains may become uniform in size), but also the EBM sample (non-uniform microstructure, as discussed above with Figure 3). The γ′ precipitates in the FZ, HAZ, and BM are uniform, exhibiting identical morphology and size. As seen in Figure 4a, they all have cubical shape with sharp vertices, straight edges, and uniform side length of about 500 nm. The γ' precipitates grow during the aging HT, becoming larger than those in the BM of the EBM sample. From the micro-indentation test results shown in Figure S3, after HT with recovery the hardness is also uniform throughout, all the way from the FZ to the HAZ and to the BM, in stark contrast to the non-uniform hardness distribution in the EBM sample due to the pronounced spatial variation of the γ' precipitates size and morphology (Figure 3a) as well as of the dislocation density. μXRD results prove that the residual strain is fully released, evidenced by the uniform light color in the 2D maps, Figure 4b. There is only slight variation in the 1D strain profile of Figure 4c. The dislocation density in the HAZ and the FZ is also brought down significantly. The TEM image in Figure 4e shows a dislocation density of 2×10^{13} m^{-2}. Multiple TEM images are taken from the HAZ, two of which are displayed in Figure S4. From these different regions the average dislocation density in the HAZ is found to be about 3×10^{13} m^{-2}, and in all local regions it never exceeds 5×10^{13} m^{-2}. In other words, compared to the as-prepared EBM sample, the dislocation density decreases by more than 20 times in the HAZ. The BM, similar to the as-prepared sample, stays dislocation free (Figure 4f).

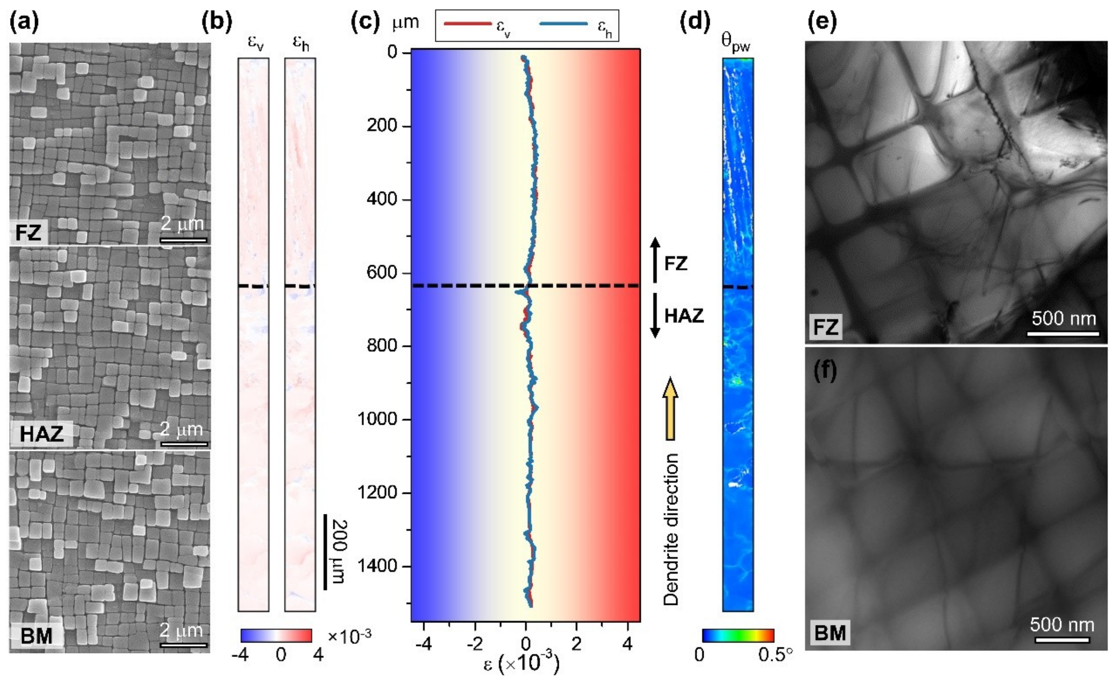

Figure 4 Uniform distributions of γ′ morphology, elastic strain and dislocations after full HT following our new protocol incorporating recovery annealing. (a) Indistinguishable SEM images of γ′ precipitates in the FZ, HAZ, and BM. μXRD proves (b, c) completely relieved strain, and (d) uniform and sharp diffraction peaks indicating low defect density (except at dendrite boundaries). The fusion line is marked with a dashed line in (b-d). TEM images indicate significant reduction in dislocation density in the HAZ (e), while BM remains almost defect free (f).

All the evidences above, including the γ′ shape, size, and micro-hardness distributions, as well as the reduced strain and dislocation density, demonstrate that our new protocol is effective in producing a uniform microstructure. The key step, absent for the standard HT, is the sub-solvus annealing at 1100 ºC for 6 h before solution treatment. It lowers the defect density that would have otherwise triggered RX during solution HT. Our discussion in the following will therefore focus on the mechanism involved to accomplish dislocation removal during this important recovery annealing step.

As shown in Figure 5, recovery annealing at 1100 ºC for 6 h leads to rafting almost everywhere in the FZ and the HAZ. Rafting is a common occurrence well known in superalloys subjected to external stresses and elevated temperatures. It can also be induced by residual stresses at certain temperatures [25]. In our case the rafted microstructure is caused by the residual stresses built-in during the EBM. The recovery annealing is carried out at a temperature close to the typical creep testing temperature for this superalloy [26]. Three typical rafted γ' microstructures (demonstrated in Figure 5a), which are recorded in the upper FZ, near the FZ/HAZ interface, and in the lower HAZ, respectively, are examined in detail. For AM3, a superalloy with negative lattice mismatch, the rafting direction is expected to be perpendicular to the tensile stress direction. In the upper FZ region, both horizontally and vertically rafted structures are observed, agreeing well with the observed spatial variation of the strain tensor and the sign (stress direction) displayed in Figure 3. Near the interface between the FZ and HAZ, vertically rafted structure forms. This is also consistent with the measured horizontal tensile strain in this region. As the strain direction reverses sign in the lower HAZ, the rafting direction changes as well. In confirmation, the strains in the recovery-annealed specimen are significantly reduced, suggesting that the elastic strain energy stored in the EBM sample is effectively released along with rafting when the γ/γ' phase boundaries migrate (Figure 5b, c). The peak width map indicates that there are residual defects in the HAZ and the lower FZ (Figure 5d), thus TEM is employed for direct observation. As shown in Figure 5e and 5f, dislocations now line up at γ/γ' phase boundaries, and dislocation networks are also observed occasionally. In the literature, these two types of dislocation configurations were reported in superalloys after creep testing [27,28]. The dislocation density near these interfaces is measured to be 9×10^{13} m^{-2} and 2×10^{14} m^{-2}, respectively, but still up to one order of magnitude lower than that in the HAZ of the EBM sample. Taken together, the μXRD and TEM observations suggest that the combined rafting-recovery is akin to that due to creep [25,29,30]. Note here again that previous annealing efforts were only able to achieve limited recovery, especially for regions that experienced rather high pre-strains in plastic deformation [31,32]. Most of the previous attempts apparently have missed the appropriate temperature window, as they were probably unaware of the potential role that could be played by the rafting of γ′ particles.

Regarding rafting, it is in fact the migration of the γ/γ′ phase boundaries that has ushered in a new mechanism to facilitate dislocation recovery. First, many dislocations sink into the interphase boundaries as they sweep by. Second, more spaces are opened for dislocation motion, as rafting widens some γ channels to accommodate dislocation movement and interactions that lead to annihilation. Third, the residual dislocations rearrange into lower-energy configurations at the γ/γ′ interfaces (Figure 5) and these aggregated dislocation bundles re-configure more readily upon subsequent solution treatment at higher temperatures, as they no longer need to run across γ′ precipitates to annihilate. This reduction of concentrated defects storing high energy leaves few spots as RX nucleation sites, such that the ensuing solution treatment no longer sets off RX.

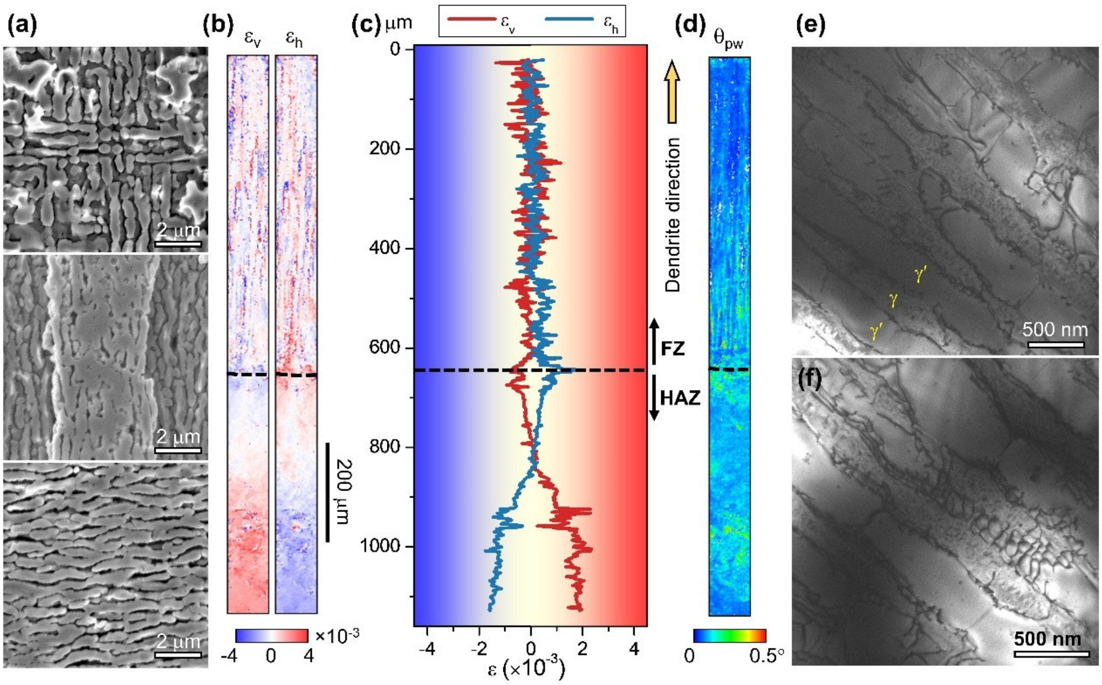

Figure 5 γ′ morphology, elastic strain and dislocations after 1100 °C recovery annealing. (a) Rafted γ′ observed in various directions. μXRD shows lowered strain in (b) 2D and (c) 1D profiles, as well as (d) reduced diffraction peak width. The fusion line is marked by dashed line in (b-d). TEM observation illustrates dislocations rearranged (e) at γ/γ′ interfaces and (f) as networks. These are presumably low-energy dislocation configurations that can readily annihilate upon solution treatment, and the dislocation densities in these two images are almost one order of magnitude lower than that in the HAZ of the EBM sample.

Discussion

The recovery HT protocol reported in this study is applicable to other 3D printing scenarios. To demonstrate this, epitaxial AM3 layers were also manufactured using the direct laser forming method on top of the cast BM with the same dimensions as those for the EBM case. The subsequent heat treatments are the same, incorporating the same recovery annealing. Homogeneous γ′ precipitates are again obtained in all the FZ, HAZ, and BM regions, without any sign of RX, as shown with EBSD examination results in Figure S5 in Supporting Information.

Furthermore, although the recovery annealing costs 6 h, it is only a minor extension to the standard HT, which involves solution treatment at 1300 ºC for 3 h followed by two steps of ageing at 1100 ºC and 870 ºC for 6 h and 20 h, respectively. The inserted recovery step is thus only a simple addition, with little additional cost while effectively curtailing the undesirable RX.

Finally, we mention in passing a tweak to the recovery approach to lower the defect density and hence the RX driving force: the substrate can be heated *in situ* along with the 3D printing (using electron beam, laser or other heating resource) process. This "preheating" may lower the temperature for recovery annealing and shorten its duration, depending on the preheating conditions. However, this substrate preheating is expected to demand a stringent temperature control: a substrate temperature too high would diminish the temperature gradient, jeopardizing the epitaxial deposition; A temperature too low, on the other hand, would still incur too much deformation in local regions and hence too many stored dislocations in the HAZ. As such one would still need to add rafting-assisted recovery to suppress RX altogether. Our results in this paper demonstrate that the delicate control of preheating is not necessary. As a limiting case, simply using post-3D-printing recovery annealing alone, with no preheating at all, is already adequate to get rid of the normally expected RX. The post-electron-beam-melting, pre-solution recovery parameters (annealing temperature and time) can be adjusted depending on the plastic strains that need to be recovered inside the printed/repaired alloy; a systematic documentation would however exceed the space limit of this Letter.

Conclusions

In summary, we have designed a new heat treatment protocol to satisfy the requirement of "no RX together with uniform γ′", mandated for 3D-printing repair of Ni-based superalloy single crystals. Most essential in our strategy is the realization of sub-solvus recovery prior to solution treatment, eliminating most of the stored defect energy that drives nucleation of new crystals during solution treatment. This is made possible by dislocation rearrangement and annihilation that are otherwise inactive in the absence of rafting γ′. Previous 3D-printing work to produce single crystalline superalloys was not aware of, and did not take advantage of, this vehicle that enables substantial recovery. Our finding thus opens an avenue to make additive manufacturing a widely applicable tool when dealing with the manufacture and repair of single-crystal superalloy part. We envision this could be used for the welding of single-crystal parts as well.

Methods

EBM with no powder feeding was carried out using a DMAMS Zcomplex3™ electron-beam 3D-printing system operated in 10^{-3} mbar vacuum. The substrate (BM) was cut into a cylinder 13 mm in diameter and 4 mm in height, from [001] cast SX boules after solid solution heat treatment. Electron beam of 15 mA was accelerated to 60 keV and focused onto the BM surface to form a melt pool. Line scanning was programmed at the velocity of 10 to 15 mm/s to ensure epitaxial dendrite growth in the melt pool. A fusion zone (FZ) of about 1500 μm in width and 800 μm in depth was generated. The EBM sample was then recovery-annealed at 1100 ºC for 6 h, solution-treated at 1300 ºC for 0.5 h, and then aged at 1100 ºC and 870 ºC for 6 h and 20 h, respectively. Note that although the solution treatment temperature was the same as the standard HT protocol, the duration needed was significantly shorter, because solute segregation in the EBM sample is much less than in its cast counterpart. Comparisons are made with an identical EBM sample heat treated without recovery, skipping the 1100 ºC annealing step. This is the standard HT sample serving as the reference.

Micro-hardness test was carried out using a Vickers hardness indenter under the force control mode, after EBM as well as after recovery annealing. On each specimen, a matrix of indentations covered the area from the BM to the FZ. Each indent was at least 4 μm deep to exclude the surface effect, and neighboring indents were 105 μm apart to make sure the hardness value was not influenced by the plastic deformation around adjacent indents.

Before and after recovery-HT, the microstructure was examined under secondary electron mode in a SEM after etching in 25% phosphoric acid water solution at the voltage of 5 V for 10 s. RX was monitored by mapping the crystal orientation of the sample surface using EBSD, after electrochemical polishing in 10% perchloric acid alcohol solution at the voltage of 20~30 V for about 60 s. μXRD sample was electro-polished the same way, and then scanned using micro-focused synchrotron polychromatic X-ray beam at the Advanced Light Source of Lawrence Berkeley

National Laboratory [33]. The collected Laue diffraction data were processed using a custom-developed software based on the peak position comparison method to measure the strain tensor distribution accurately [34]. The defect density maps were obtained semi-quantitatively by plotting the Laue peak width distribution [35]. TEM specimens were prepared using the conventional twin-jet electropolishing.

Acknowledgements

This work is supported by the National Natural Science Foundation of China (Grant No. 91860109, 51901026), and the National Key Research and Development Program of China (Grant No. 2016YFB0700404). We also appreciate the support from the International Joint Laboratory for Micro/Nano Manufacturing and Measurement Technologies. E.M. is supported at JHU by NSF-DMR-1804320. The ALS was supported by the Director, Office of Science, Office of Basic Energy Sciences, Materials Science Division, of the U.S. Department of Energy under Contract No. DE-AC02-05CH11231 at LBNL. JL acknowledges support by NSF CMMI-1922206.

Author contributions

K.C., E.M., Z.W.S. and J.L. designed the project. R.H. conducted the EBM and direct laser forming experiments. R.H. and Y.L. developed the HT protocol for the EBM specimens. S.L. performed the HT on the direct laser forming sample. W.Z. carried out TEM and μXRD characterizations, and then analyzed and interpreted the μXRD data with R.H. under the supervision of K.C. and N.T. The paper was written by K.C., R.H., E.M., Z.W.S. and J.L. All authors contributed to discussions of the results.

References:

1. Pollock, T. M. Alloy design for aircraft engines. *Nat. Mater.* **15**, 809–815 (2016).
2. Koff, B. L. Gas turbine technology evolution: A designers perspective. *J. Propuls. power* **20**, 577–595 (2004).
3. Babu, S. S. *et al.* Additive manufacturing of nickel superalloys: Opportunities for innovation and challenges related to qualification. *Metall. Mater. Trans. A* **49**, 3764–3780 (2018).
4. Gäumann, M., Henry, S., Cléton, F., Wagnière, J.-D. & Kurz, W. Epitaxial laser metal forming: analysis of microstructure formation. *Mater. Sci. Eng. A* **271**, 232–241 (1999).
5. Gäumann, M., Bezençon, C., Canalis, P. & Kurz, W. Single-crystal laser deposition of superalloys: Processing-microstructure maps. *Acta Mater.* **49**, 1051–1062 (2001).
6. Vitek, J. M. The effect of welding conditions on stray grain formation in single crystal welds – theoretical analysis. *Acta Mater.* **53**, 53–67 (2005).
7. Ramsperger, M. & Körner, C. Selective Electron Beam Melting of the Single Crystalline Nickel-Base Superalloy CMSX-4®: From Columnar Grains to a Single Crystal. in *Superalloys 2016* 341–349 (2016).
8. Liang, Y. J. *et al.* Experimental optimization of laser additive manufacturing process of single-crystal nickel-base superalloys by a statistical experiment design method. *J. Alloys Compd.* **697**, 174–181 (2017).
9. Liang, Y.-J., Cheng, X., Li, J. & Wang, H.-M. Microstructural control during laser additive

manufacturing of single-crystal nickel-base superalloys: New processing–microstructure maps involving powder feeding. *Mater. Des.* **130**, 197–207 (2017).

10. Körner, C. *et al.* Microstructure and Mechanical Properties of CMSX-4 Single Crystals Prepared by Additive Manufacturing. *Metall. Mater. Trans. A* **49**, 3781–3792 (2018).
11. Basak, A., Acharya, R. & Das, S. Epitaxial deposition of nickel-based superalloy René 142 through scanning laser epitaxy (SLE). *Addit. Manuf.* **22**, 665–671 (2018).
12. Gorsse, S., Hutchinson, C., Gouné, M. & Banerjee, R. Additive manufacturing of metals: a brief review of the characteristic microstructures and properties of steels, Ti-6Al-4V and high-entropy alloys. *Sci. Technol. Adv. Mater.* **18**, 584–610 (2017).
13. Chauvet, E. *et al.* Hot cracking mechanism affecting a non-weldable Ni-based superalloy produced by selective electron Beam Melting. *Acta Mater.* **142**, 82–94 (2018).
14. Ramsperger, M., Lopez-Galilea, I., Singer, R. F., Theisen, W. & Körner, C. Solution heat treatment of the single crystal nickel-base superalloy CMSX-4 fabricated by selective electron beam melting. *Adv. Eng. Mater.* **17**, 1486–1493 (2015).
15. Tadano, S., Hino, T. & Nakatani, Y. A modeling study of stress and strain formation induced during melting process in powder-bed electron beam melting for Ni superalloy. *J. Mater. Process. Technol.* **257**, 163–169 (2018).
16. Yu, X. X. & Wang, C. Y. The effect of alloying elements on the dislocation climbing velocity in Ni: A first-principles study. *Acta Mater.* **57**, 5914–5920 (2009).
17. Tian, C., Han, G., Cui, C. & Sun, X. Effects of stacking fault energy on the creep behaviors of Ni-base superalloy. *Mater. Des.* **64**, 316–323 (2014).
18. Shang, S. L. *et al.* Effects of alloying element and temperature on the stacking fault energies of dilute Ni-base superalloys. *J. Phys. Condens. Matter* **24**, (2012).

19. Humphreys, F. & Hatherly, M. *Recrystallization and Related Annealing Phenomena*. (Elsevier, 2004).

20. Li, Z., Xu, Q. & Liu, B. Microstructure simulation on recrystallization of an as-cast nickel based single crystal superalloy. *Comput. Mater. Sci.* **107**, 122–133 (2015).

21. Bürgel, R., Portella, P. D. & Preuhs, J. Recrystallization in single crystals of nickel base superalloys. in *Superalloys 2000* **5**, 229–238 (2000).

22. Li, Z. L., Xu, Q. Y., Xiong, J. C., Li, J. R. & Liu, B. C. Plastic Deformation and Recrystallization of a Ni-Based Single Crystal Superalloy. in *Materials Science Forum* **850**, 47–55 (2016).

23. Cox, D. C., Roebuck, B., Rae, C. M. F. & Reed, R. C. Recrystallisation of single crystal superalloy CMSX–4. *Mater. Sci. Technol.* **19**, 440–446 (2003).

24. Li, Y., Chen, K. & Tamura, N. Mechanism of heat affected zone cracking in Ni-based superalloy DZ125L fabricated by laser 3D printing technique. *Mater. Des.* **150**, 171–181 (2018).

25. Nabarro, F. R. N. Rafting in superalloys. *Metall. Mater. Trans. A* **27**, 513–530 (1996).

26. Steuer, S. *et al.* Creep behavior under isothermal and non-isothermal conditions of AM3 single crystal superalloy for different solutioning cooling rates. *Mater. Sci. Eng. A* **601**, 145–152 (2014).

27. Zhang, J. X., Wang, J. C., Harada, H. & Koizumi, Y. The effect of lattice misfit on the dislocation motion in superalloys during high-temperature low-stress creep. *Acta Mater.* **53**, 4623–4633 (2005).

28. Dirand, L. *et al.* Measurement of the effective γ/γ′ lattice mismatch during high temperature creep of Ni-based single crystal superalloy. *Mater. Charact.* **77**, 32–46 (2013).

29. Kamaraj, M. Rafting in single crystal nickel-base superalloys - An overview. *Sadhana* **28**, 115–128 (2003).

30. Matan, N., Cox, D. C., Rae, C. M. F. & Reed, R. C. On the kinetics of rafting in CMSX-4 superalloy single crystals. *Acta Mater.* **47**, 2031–2045 (1999).

31. Bond, S. D. & Martin, J. W. Surface recrystallization in a single crystal nickel-based superalloy. *J. Mater. Sci.* **19**, 3867–3872 (1984).

32. Xie, G., Zhang, J. & Lou, L. H. Effect of cyclic recovery heat treatment on surface recrystallization of a directionally solidified superalloy. *Prog. Nat. Sci. Mater. Int.* **21**, 491–495 (2011).

33. Kunz, M. *et al.* A dedicated superbend x-ray microdiffraction beamline for materials, geo-, and environmental sciences at the advanced light source. *Rev. Sci. Instrum.* **80**, (2009).

34. Tamura, N. XMAS: A Versatile Tool for Analyzing Synchrotron X-ray Microdiffraction Data. in *Strain and Dislocation Gradients from Diffraction: Spatially-Resolved Local Structure and Defects* (eds. Barabash, R. & Ice, G.) 125–155 (World Scientific, 2014).

35. Kou, J., Chen, K. & Tamura, N. A peak position comparison method for high-speed quantitative Laue microdiffraction data processing. *Scr. Mater.* **143**, 49–53 (2018).